communications physics

Article

https://doi.org/10.1038/s42005-024-01593-x

Momentum-dependent intraband high harmonic generation in a photodoped indirect semiconductor

Pawan Suthar [1], František Trojánek [1], Petr Malý[1], Thibault J.-Y. Derrien [2] & Martin Kozák [1]

Nonlinear optical response of solid-state materials exposed to strong non-resonant light fields leads to the generation of harmonic frequencies as a consequence of interband polarization and coherent intraband dynamics of the electrons. The efficient production of a macroscopic wave requires the preservation of the mutual phase between the driving wave and the individual microscopic sources of radiation. Here, we experimentally and theoretically show that the yield of high harmonic generation in a photodoped silicon crystal is enhanced by the nonlinear intraband current whose amplitude depends not only on the volume density of the photogenerated carriers but also on their momentum distributions within the bands. The strongest enhancement is reached when the carrier system is relaxed to the band minima before interacting with the strong nonresonant wave, which drives the high harmonic generation. These results extend the possibilities of high harmonic spectroscopy towards the investigation of ultrafast carrier relaxation in condensed matter.

Strong-field nonlinear optics has allowed to control the electron dynamics on time scales shorter than the individual oscillations of light waves[1–3]. A general feature of all nonlinear optical interactions is the emission of light at harmonic frequencies of the driving wave frequency resulting from the anharmonic motion of the electrons driven by the incident field. High harmonic generation (HHG) in atoms has been widely applied as a broadband source of coherent extreme ultraviolet radiation and isolated attosecond pulses[1–4]. HHG in atoms follows the three-step model[4,5], which includes dynamical tunneling of the electron, propagation in the laser field, and re-collision with the parent ion leading to the emission of high-energy photons.

Recently, HHG in solids has seen rapid progress towards compact light sources and solid-state attosecond metrology[6–26]. HHG in condensed matter differs from the atomic case in two main aspects. The first difference is the presence of an additional intraband source of harmonic emission related to the anharmonic motion of electrons accelerated in non-parabolic bands of the material. The intraband dynamics[8,16,27,28] and coherent interband polarization[15,29,30] have both been found to contribute to the harmonic emission in solids. The relative strengths of these two contributions vary depending on the material, driving frequency, and other experimental parameters[17,21,26,27,31]. The second difference between HHG in solids and atoms is the presence of momentum scattering during propagation of the electron-hole wavepacket in a material with high density of surrounding atoms and valence electrons. Theoretical predictions[32] and experimental results[15,33–36] suggest that the related dephasing time can be as short as few femtoseconds for high energy electrons, which is comparable or even shorter time than one period of the oscillating electric field, which drives the HHG process. Once the electron loses its phase relation with other coherently oscillating charges, it cannot further contribute to the macroscopic HHG and the amplitudes of both the interband polarization and the coherent intraband current decrease leading to suppression of the HHG yield.

The rate of electron-electron scattering and the amplitude of the coherent intraband current can be probed by photodoping the crystal prior to the interaction with the strong nonresonant pulse using a resonant optical excitation. The excited carriers affect the high harmonic generation process in two ways. The first effect, which has already been observed and which is not the main topic of this study, is the decrease of the high harmonic yield due to dephasing of electron-hole wavepackets[15,33–35]. When this mechanism of HHG suppression is dominant, the higher order harmonics are suppressed more than the lower harmonic frequencies[33–35]. The second effect of photodoping on the HHG is the increase of the macroscopic intraband current which enhances the HHG yield[34]. After the resonant photodoping, the excess carriers in the material are subsequently accelerated by the oscillating electric field of the strong pulse coming with a certain time delay after the resonant excitation. Due to their coherent accelerated motion in the

[1]Faculty of Mathematics and Physics, Charles University, Ke Karlovu 3, 12116 Prague 2, Czech Republic. [2]HiLASE Centre, Institute of Physics, Academy of Science of the Czech Republic, Za Radnicí 828/5, 25241 Dolní Břežany, Czech Republic. e-mail: m.kozak@matfyz.cuni.cz

non-parabolic bands, these carriers emit photons at harmonic frequencies of the driving field enhancing the HHG signal. Both these effects, i.e., the suppression due to a higher dephasing rate and an enhancement due to the additional intraband current, affect the coherent emission of photons with energy both below and above the band gap of the material. The final change of the harmonic yield induced by photodoping can be interpreted as a result of the interplay of the two phenomena.

Here, we demonstrate that the additional intraband contribution to the high harmonic generation depends not only on the volume density of photodoped carriers but also on their momentum distribution in the instant of time when the strong HHG driving pulse arrives to the sample. The amplitude and phase of the intraband high harmonic radiation emitted by each charge carrier depends on its initial momentum state, which in combination with the shape of the surrounding energy band determines its real space trajectory. As a consequence, the macroscopic intraband current is a function of the momentum distribution of charge carriers at the moment of impact of the strong infrared pulse on the crystal.

Results and discussion

The role of momentum distribution of excess carriers in the intraband HHG is studied using high harmonic spectroscopy in a photodoped silicon crystal (see the sketch of the experimental setup in Fig. 1a, the experimental details are described in Methods). The yield of HHG is measured as a function of the time delay between a resonant pulse which excites free electron hole pairs in silicon and a strong infrared pulse which generates the harmonics. To vary the initial energy and momentum distribution of resonantly excited carriers we use two distinct photon energies of photodoping pulses, namely 1.8 eV and 3.6 eV, respectively. The strong infrared pulse which drives the HHG has photon energy of 0.62 eV, pulse duration of 30 fs and peak intensity of ≈2 TW/cm^2 (the peak intensity of the HHG driving pulse is kept the same in all the experiments). Under these conditions, HHG in silicon occurs in the strong-field regime[30]. The measured HHG spectra after photodoping with pulses at photon energy of 3.6 eV are shown in Fig. 1b for three different values of the time delay (negative time delay corresponds to the earlier arrival of the HHG driving pulse and thus to HHG in silicon without photodoping). We observe that the HHG yield drops strongly in a short time after photodoping for all harmonics, with the decrease being larger for higher harmonic frequencies. The minimum corresponding to the red curve in Fig. 1b is reached in the time delay of 200 fs. The yields of all harmonic orders then increase on time scale of ≈3 ps (blue curve in Fig. 1b). The measured dependence of the normalized high harmonic yield on the time delay between the photodoping and the driving pulses is shown in Fig. 1c, d for the photon energies of the photodoping pulses of 3.6 eV and 1.8 eV, respectively. We observe strikingly different initial dynamics of the HHG yield for these two cases. When the carriers are excited by photons with energy of 1.8 eV, the HHG yield changes its value at short time delay after the photodoping but no significant subsequent increase of the yield is observed within the first 5 ps. This behavior is similar to previous observations[15], in which the HHG yield changed suddenly after photodoping of the crystal and its slow dynamics can be attributed to carrier recombination. In silicon, the carrier recombination occurs on timescales of tens to hundreds of picoseconds (the slow component of the change of the

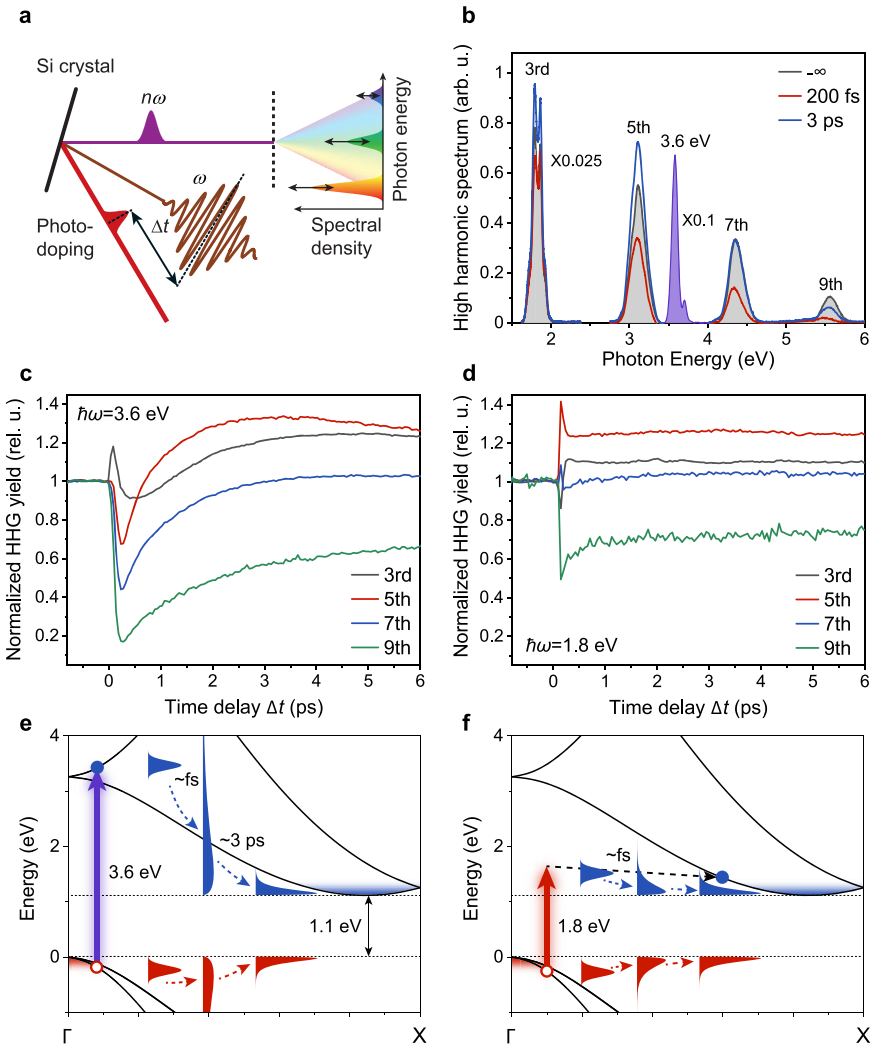

Fig. 1 | Dependence of high harmonic generation in silicon on the energy and momentum distributions of photodoped carriers. a Layout of the experimental setup for the measurement of high harmonic spectra in a photodoped Si crystal. **b** High harmonic spectra of silicon measured at different time delays between the photodoping and strong-field pulses. Time delay -∞ corresponds to the case, in which the strong infrared pulse arrives earlier than the photodoping pulse (the harmonics are produced in an unexcited sample). Measured evolution of the high harmonic generation yield of different harmonic frequencies in silicon as a function of the time delay Δt between resonant photodoping with photons at the energy of 3.6 eV (**c**) or 1.8 eV (**d**) and the strong infrared pulse which drives the high harmonic generation. Excited carrier density generated by photodoping is $N_d = 2.75 \times 10^{21}$ cm^{-3} at 3.6 eV and $N_i = 6 \times 10^{19}$ cm^{-3} at 1.8 eV. Peak irradiance of the strong infrared pulse is 2 TW/cm^2. Band structure of silicon along $\mathbf{k}_x$ direction (Γ-X) with the outline of the electron-hole dynamics following photoexcitation with photon energy of 3.6 eV (**e**) and 1.8 eV (**f**).

HHG yield is shown in Supplementary Note 1 with both photon energies of photodoping pulses) while the characteristic time scales of carrier relaxation is 200–300 fs (time after which the effective carrier temperature decreases to $1/e$ of its initial value)[37,38].

To understand the observed differences in the initial dynamics shown in Fig. 1c, d, we need to focus on the band structure of silicon and the difference in the energy and momentum distributions of electrons and holes excited by 3.6 eV and 1.8 eV photon energies. Silicon has an indirect band structure with six times energy degenerate minima of the conduction band located close to the X-point of the Brillouin zone and the maximum of the valence band in the Γ-point. The width of the indirect band gap is 1.12 eV while the width of the first direct band gap in the Γ-point ($\mathbf{k} = 0$) is about 3.4 eV. Silicon band structure along the Γ-X direction ($\mathbf{k}_x$) is shown in Fig. 1e, f together with the visualization of the direct and indirect excitation paths induced by photodoping with photons at the energies of 3.6 eV and 1.8 eV, respectively. The momentum and energy distributions of the electrons and holes shortly after the excitation (blue and red profiles in Fig. 1e, f) differ strongly for the two excitation paths. While the electron-hole pairs have an average excess energy of $E_{ex} \sim 2.5$ eV for the direct excitation by photons with the energy of 3.6 eV, the excess energy is only $E_{ex} \sim 0.6$ eV for the excitation by 1.8 eV photons (~50 meV per electron-hole pair is lost due to emission of a phonon necessary to conserve momentum during an indirect transition). Thermal equilibrium is established in the system of excited electrons and holes within a few tens of femtoseconds to approx. 150 femtoseconds after the resonant excitation via electron-electron scattering due to Coulomb interaction between the excited carriers[39]. Immediately after the thermalization, the carrier distribution function in the i-th band f_i can be approximated by a product of the density of states and Maxwell-Boltzmann distribution. The latter is associated to an effective carrier temperature, which is initially well above the temperature of the crystal lattice. When assuming equal splitting of the excess kinetic energy between an excited electron and hole (the average excess energy of each quasiparticle is one half of the excess energy of the electron-hole pair), the effective temperature of carriers can be estimated as $T_{eff} = E_{ex}/(3k_B) = 9700$ K for 3.6 eV photodoping and $T_{eff} = 2500$ K for 1.8 eV photodoping. Our experimental results suggest that the yield of coherent intraband emission generated by the photodoped carriers accelerated by the infrared field depends on the effective temperature of the carrier system in the time of arrival of the strong infrared driving pulse.

The initial fast dynamics observed with photodoping via the direct path is additionally influenced by two other phenomena. The first effect is related to the high density of photodoped carriers excited by 3.6 eV photons, which is $N_d = 2.75 \times 10^{21}$ cm^{-3}. This is much higher value compared to the carrier density excited by 1.8 eV photons of only $N_i = 6.0 \times 10^{19}$ cm^{-3}. The density excited by the direct transition is in the regime, where state filling, band gap renormalization and free carrier response change the dielectric constant of silicon leading to a decrease of surface reflectivity[40], which probably influences also the yield of the reflected high harmonic radiation (dependence of harmonic yield on photodoped carrier density is shown in Supplementary Note 4, Supplementary Fig. 4). The second difference between the direct and indirect excitation paths lies in the spatial profiles of excited carriers in the crystal (dependence of the excited carrier density on the depth in the crystal). While the absorption coefficient is $\alpha_i = 2.35 \times 10^3$ cm^{-1} for the indirect transition at 1.8 eV leading to the penetration depth of light of about 4 μm, its value grows to $\alpha_d = 1.09 \times 10^6$ cm^{-1} for the direct transition at 3.6 eV[41] corresponding to the penetration depth of only 9 nm. The high spatial gradient of carrier density immediately after the photodoping in the latter case leads to rapid diffusion and a fast decrease of the density in the region close to the crystal surface. The numerical solution of diffusion equation suggests a rapid decrease of the carrier density in the surface silicon layer within the first 1 ps after the photodoping (see Supplementary Note 2 and Supplementary Fig. 2). Such a rapid decrease probably influences the observed initial fast dynamics of the increase of HHG yield with 3.6 eV photodoping because the harmonics are mainly generated in a thin surface layer with a thickness of few tens of nanometers (phase-matching considerations for reflected harmonics are discussed in Supplementary Note 3 and Supplementary Fig. 3).

To separate the dynamics caused by the dependence of the additional intraband HHG on the carrier momentum distribution from the dynamics induced by high density effects and/or carrier diffusion we prepare the electron-hole system to a state, in which both the direct and indirect transitions are present with the depth profiles of the excited carrier density decaying on μm scale. This is achieved by using spectrally broadened and compressed photodoping pulses at 1.8 eV with peak intensity high enough to allow carrier excitation by direct two-photon absorption simultaneously with single-photon indirect absorption channel. To characterize the carrier density generated by two-photon absorption we measure the value of the two-photon absorption coefficient $\beta = 3.0$ cm/GW using z-scan technique[42] (for details see Supplementary Note 6 and Supplementary Fig. 5). The maximum density of carriers excited by the combination of single- and two-photon absorption processes in our experiments can be estimated as $N_0 = (1-R)F_0/(\hbar\omega)\left[\alpha + \beta(1-R)F_0/(2\sqrt{2\pi}\tau)\right] = 2.11 \times 10^{20}$ cm^{-3}, where $N_i^{(1ph)} = 1.52 \times 10^{20}$ cm^{-3} and $N_d^{(2ph)} = 0.59 \times 10^{20}$ cm^{-3} are the populations generated by the single-photon indirect and two-photon direct processes, F_0 is the peak fluence, τ is pulse duration, $\hbar\omega$ is photon energy and R is Fresnel reflectivity of silicon (details on calculations of the excited carrier density can be found in Supplementary Note 5). The measured dynamics of the 5th harmonic yield after the combined single- and two-photon photodoping is shown in Fig. 2 for different fluences of the photodoping pulses. The spatial distribution of excited carriers decays on several micrometer length scale for both types of transitions and the diffusion thus does not play a significant role in the initial picosecond dynamics. We observe that with low fluence of the photodoping pulse, at which the two-photon excitation is suppressed and the electrons and holes are only excited via single-photon indirect transition close to the band minima, the change of the HHG yield is instantaneous and the picosecond growth of the signal corresponding to an increase of the macroscopic intraband current due to carrier relaxation is not present. In contrast, with high fluence of the photodoping pulse, the picosecond increase of the harmonic yield is observed for all harmonic orders. This increase corresponds to the macroscopic intraband emission generated by the carriers, which are excited via two-photon transition and relax to the band minima within approximately 3–5 ps after the excitation. For the combination of indirect single-photon and direct two-photon excitations, the effective temperature of carriers depends on the fluence of the photoping pulse because the ratio of carrier densities excited by the two distinct transitions scales linearly with the fluence. We note that the coherent signal (short spike at zero time delay), which is present when the two pulses are overlapped in time on the sample, is coming from the coherent frequency mixing of the two pulses. The presence of the two-photon absorption process induced by 1.8 eV pump is additionally verified by measuring the amplitude of the picosecond component of the HHG yield dynamics of individual harmonic frequencies as a function of the fluence of the photodoping pulse. The observed quadratic dependence is shown in Fig. 2b, where the fast signal component corresponds to the difference between the signal values in the time delays of 3 ps and 200 fs. The initial effective carrier temperature at the maximum fluence of the photodoping pulse can be estimated as $T_{eff} = 5000$ K.

In the following, we introduce a simple model explaining the observed dependence of the intraband HHG on the initial momentum distribution of pre-excited carriers. The amplitude and phase of intraband harmonics emitted by an individual charge carrier accelerated in a band by a coherent oscillating electric field can be calculated using single electron model as a function of the initial momentum of the electron(hole) $\mathbf{k}_0$. When we neglect the electron scattering during the acceleration by the HHG driving pulse and the interband transitions (this approximation is only used to illustrate the dependence of the amplitude and phase of the intraband HHG on the initial electron momentum), the reciprocal space trajectory is determined by Bloch's acceleration theorem $\dot{\mathbf{k}} = -q\mathbf{F}(t)/\hbar$, where q is the electric charge, $\mathbf{F}(t)$ is the time-dependent electric field amplitude of the strong infrared

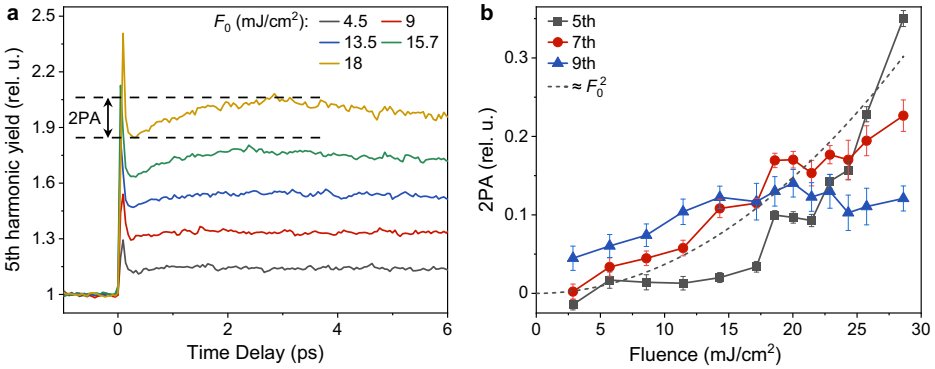

Fig. 2 | Dynamics of the yield of high harmonic generation with simultaneous photodoping by single- and two-photon absorption of 1.8 eV photons. a The curves correspond to the yield of 5th harmonic generation for different values of peak fluence F_0 of the photodoping pulse. The arrow indicates the amplitude of the picosecond signal component, which increases nonlinearly with the increasing fluence and which is generated by carriers excited via two-photon absorption (2PA). **b** The amplitude of the picosecond component of the HHG yield change corresponding to two-photon absorption for 5th harmonics (black squares), 7th harmonics (red circles) and 9th harmonics (blue triangles). The measured data are compared to the quadratic function of fluence (dashed curve). The error bars correspond to the standard deviation of the data of each curve in (**a**) at time delays below zero.

pulse and $\mathbf{k}$ is crystal momentum. The solution can be written using the vector potential $\mathbf{A}(t) = \int_{t_0}^{t} \mathbf{F}(t')dt'$ as $\mathbf{k}(t) = \mathbf{k}_0 + q\mathbf{A}(t)/\hbar$. The real space velocity of an electron wavepacket in i-th band with energy dispersion $E_i(\mathbf{k})$ is calculated as $\dot{\mathbf{r}} = \nabla_{\mathbf{k}} E_i(\mathbf{k})/\hbar$ and it is proportional to the single electron intraband current $\mathbf{j}_i(t) = q\dot{\mathbf{r}}$. The associated emission spectrum generated by the oscillating charge is obtained by using Larmor formula $S(\omega) = \omega^2|\mathcal{FT}\{j(t)\}|^2$. When we consider a 1D model with an arbitrary shape of the band structure, we can approximate the electron dispersion in the vicinity of the initial electron momentum k_0 using Taylor series as $E_i(k) = E_i(k_0) + \sum_{n=1}^{\infty} E_i^{(n)}(k_0)(k-k_0)^n/n!$, where the superscript (n) stands for n-th derivative with respect to k. From this we can directly calculate the intraband current generated by the electron as:

$$j(t) = q\sum_{n=1}^{\infty} E_i^{(n)}(k_0)n(qA(t)/\hbar)^{n-1}/n!. \quad (1)$$

The current obtained by Eq. (1) is a sum of integer powers of the vector potential of the strong infrared pulse $A(t)$. The Fourier transform of the term with the power $(n-1)$ contains odd or even order harmonic frequencies up to the order $(n-1)$ with the amplitude proportional to the particular derivative order of the band dispersion $E_i^{(n)}(k_0)$. Because each harmonic frequency is not generated only by a single term but also by higher powers of the vector potential, the amplitude corresponds to the superposition of all the contributing terms. From this simple analysis we see that in general, the harmonic spectrum generated by intraband acceleration of a single electron is a function of its initial momentum k_0 because it is determined by the shape of the band in its vicinity.

To describe the dependence of the additional macroscopic intraband HHG on the initial momentum distribution of an ensemble of pre-excited carriers in silicon we consider the acceleration of electrons and holes in light and heavy hole valence bands and the lowest conduction band of silicon along $\mathbf{k}_x$-direction. Because of the strong anisotropy of the electron effective masses (in Fig. 3a, we show the 1st Brillouin zone of silicon with constant energy surfaces in the vicinity of the conduction band minima) combined with the fact that the applied electric field has polarization along x direction, we approximate the lowest electron band by two parts, namely the conduction band along the line $k_y = 0, k_z = 0$ and the four-times degenerated band going through the conduction band minima in the direction of the transverse effective mass (red arrows in Fig. 3a). The bands included in the model are shown in Fig. 3b. The single electron trajectories are determined using the analysis described above and the total current of the electron-hole distribution is calculated as $j_i(t) = \int_{BZ} \dot{\mathbf{r}} f_i(\mathbf{k}_0)d^3\mathbf{k}$. Here $f_i(\mathbf{k}_0)$ is the electron and hole distribution in the i-th band in the time of arrival of the strong infrared pulse (details can be found in Methods). The HHG spectrum is obtained using Larmor formula from the total intraband current $j(t) = \sum_i j_i(t)$. Carrier momentum scattering during the interaction with the HHG driving pulse is neglected. We note that this approximation does not influence the results because once the carrier loses its phase with respect to the driving field, it cannot further contribute to the coherent high harmonic radiation. Ultrafast scattering occurring during the short period of time when the electron is accelerated by the strong infrared pulses (time duration of 30 fs) described by a single phenomenological coherence time T_2 would thus only lead to a decrease of the harmonic yield but it would not influence the dependence of the yield on the initial momentum distribution of carriers.

The spectra of the intraband HHG calculated using the 1D semiclassical model are shown in Fig. 3c for three values of the effective temperature of the carrier system in the time of arrival of the strong infrared pulse. The calculated HHG yield of the 5th, 7th and 9th harmonics are shown in Fig. 3d as a function of the effective carrier temperature (the signal of each harmonics is calculated by integrating the spectral window with the width of 0.1 eV in Fig. 3c. Here, we see that the decrease of the calculated HHG yield with higher initial carrier temperature is stronger at higher photon energies. This is in agreement with our experimental observations, in which the HHG yield of higher harmonic frequencies is increasing at longer time scales (requires lower effective carrier temperature) then the yield of lower order harmonics. We note that the quantum-mechanical description is not necessary in this case because the electron-hole system looses the quantum-mechanical coherence during the energy relaxation within the first few tens of femtoseconds after photodoping. For this reason, any effects related to the quantum mechanical phase acquired by the incoherent electron distribution driven by the strong infrared pulse are not expected. Our model brings only a qualitative understanding to the observed effects. Quantitative calculations of the dependence of the intraband HHG on carrier momentum distribution require more advanced theory, possibly based on semiconductor Bloch equations. However, the application of this method for the description of HHG in silicon is not straightforward due to the large number of bands involved, for which the dipole moments of individual interband transitions would have to be calculated and taken into account.

Conclusions

Our experimental results show that it is possible to clearly separate the intraband contribution to the HHG induced by pre-excited carriers accelerated by low-frequency strong field from the interband and intraband harmonics generated solely by the strong infrared pulse in an indirect band gap material. The sign of the change of the HHG yield induced by photodoping depends on the interplay between the electron dephasing causing a decrease of the HHG yield and the macroscopic intraband current leading to

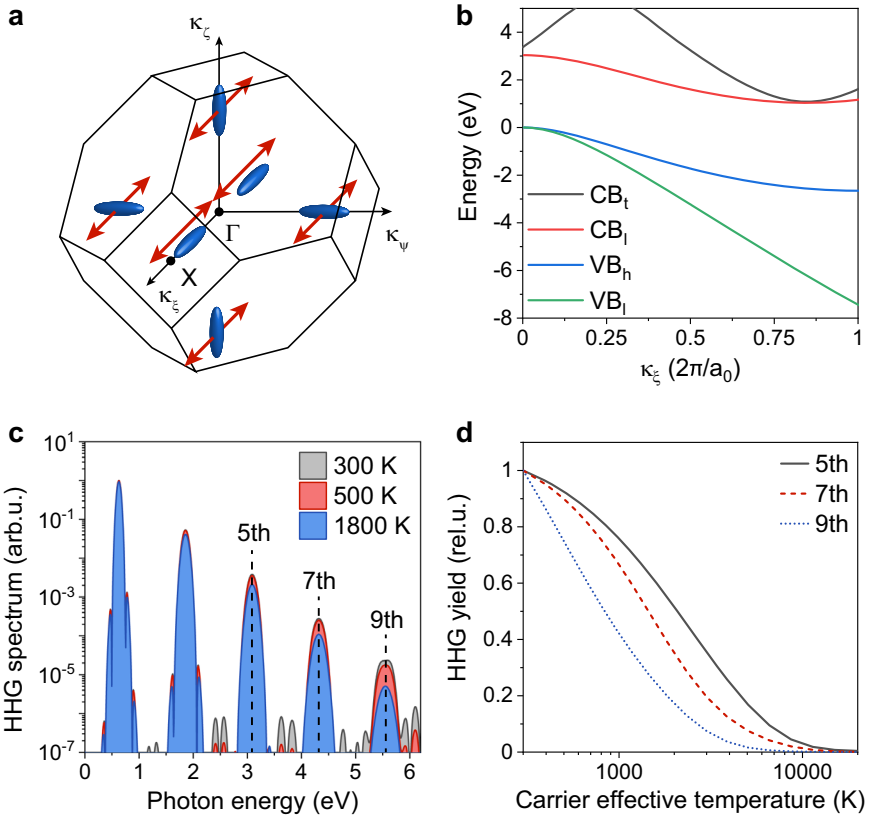

Fig. 3 | Numerical calculations of intraband high harmonic generation in photodoped silicon using semi-classical 1D model. a Brillouin zone of silicon with six energy degenerated minima of the conduction band (ellipsoids of constant energy are shown). Red arrows show the direction of the applied oscillating electric field. **b** Dispersion of two hole and two electron bands used in the 1D model of intraband high harmonic generation (see Methods for details). **c** High harmonic spectra corresponding to macroscopic nonlinear intraband current generated by acceleration of pre-excited electrons and holes by the strong infrared pulse with photon energy of 0.62 eV, duration of 20 fs and peak electric field of $F_0 = 2.3$ GV/m in silicon for three different effective temperatures of the electron-hole system. **d** The calculated yield of intraband high harmonic generation for 5th (solid curve), 7th (dashed curve) and 9th (dotted curve) harmonics as a function of the effective temperature of the electron-hole system.

an enhancement of the generation yield. The observed dependence of the intraband HHG on the initial momentum distribution of carriers can be applied to study the ultrafast electron dephasing and carrier relaxation in condensed matter and thus extends the capabilities of solid-state high harmonic spectroscopy. Moreover, the possibility of accelerating the charge carriers along specific directions by controlling the polarization state of the strong driving wave may reveal anisotropic distribution of electrons in conduction bands of solid-state crystals with multiple energy degenerate conduction band minima.

Methods

Experimental setup

The HHG spectra are measured in reflection geometry to avoid nonlinear propagation effects on the mid-infrared pulse, which drives the HHG. The setup is based on a non-collinear pump-probe scheme with the resonant pulses at photon energies of 1.8 eV (wavelength of 690 nm, duration of 50 fs) and 3.6 eV (345 nm, 50 fs), respectively, and the mid-infrared (MIR) driving pulses with photon energy of 0.62 eV (2000 nm) and pulse duration of 30 fs. The MIR pulses are generated in non-collinear optical parametric amplifier —difference frequency generation setup pumped by a ytterbium femtosecond laser (Pharos SP, Light Conversion)[43]. The pulses used for resonant photodoping at photon energy of 1.8 eV are generated in an independent non-collinear optical parametric amplifier (NOPA), which is frequency doubled in a BBO crystal for generation of 3.6 eV photons. The time delay between the resonant pump and MIR probe pulses is controlled using an optical delay stage. The pulses used to excite the carriers via the combination of single- and two-photon transitions are generated in the NOPA with broader spectrum and are compressed to the duration of 12 fs (measured with SPIDER - spectral-phase interferometry for direct electric field reconstruction[44]).

The pump and probe pulses are tightly focused using two parabolic mirrors with focal distances of $f = 50$ mm. The high harmonics produced at the front surface of the silicon sample by the MIR beam with angle of incidence of $\theta = 10^{\circ}$ are detected using a grating spectrometer (Andor Shamrock 163) with an actively cooled charge-coupled device camera (Andor iDUS 420). The incidence angle of the resonant pump beam is different to allow spatial filtering of the harmonic signal from the reflected pump (see Fig. 1a). The higher order frequency mixing components between the pump and probe light, which are generated when the two pulses overlap in time in the sample, are spatially separated from the HHG beam and are not detected (only a small fraction of scattered light is detected at zero time delay of some of the measurements).

Semi-classical 1D model of intraband high harmonic generation in silicon

The model is used to describe the part of the harmonic radiation, which is generated only by the carriers, which are first excited in the silicon band structure by the resonant photodoping pulse. After establishing thermal equilibrium via electron-electron interaction, the electrons and holes are accelerated by a strong oscillating electric field of an infrared pulse leading to macroscopic intraband current associated with HHG emission. The dynamics are approximated by a 1D model of silicon band structure, which is obtained as a cut through the minima of the conduction band and the maxima of the light and heavy hole bands in k_x-direction (dispersion of bands used in the model is shown in Fig. 3b). Silicon band structure is calculated using density functional theory with TB09 functional (details can be found in ref. 30). The energy dispersion of individual i-th band is approximated by its Fourier decomposition as $E_i(k) = \sum_{n=0}^{13} a_{i,n} \cos(2\pi n/\Lambda_{i,n})$, where the coefficients $a_{i,n}$ and $\Lambda_{i,n}$ are obtained from the least squares fit of the numerically calculated band structure. This procedure allows us to describe the band dispersion and its derivative with respect to quasi-momentum analytically. In each band we assume a system of thermalized carriers with an effective temperature T_{eff}. The momentum-dependent population is described using Maxwell-Boltzmann distribution function:

$$f(E_i(k), T_{\mathrm{eff}}) = g_i \left(\frac{m_{i,\mathrm{eff}}}{2\pi k_{\mathrm{B}} T_{\mathrm{eff}}} \right)^{3/2} e^{-\frac{|E_i(k) - E_i(k_0)|}{k_{\mathrm{B}} T_{\mathrm{eff}}}}. \quad (2)$$

Here g_i is the degeneracy factor of i-th band, $m_{i,\mathrm{eff}}$ is the effective mass associated with i-th band and k_0 is the momentum corresponding to the minimum (maximum) energy of the conduction (valence) band. In our model we neglect the carrier recombination because it occurs on much longer time scales then the picosecond relaxation dynamics (long component of the measured dynamics of HHG yield is plotted in Supplementary Fig. 1). The distribution function described using Eq. (2) leads to constant total carrier population in each band $N_i(T_{\mathrm{eff}}) = \int_0^\infty f(E_i(k), T_{\mathrm{eff}})d^3k$ in parabolic approximation, in which the dispersion close to band minima can be described as $E_i(k) = \hbar^2k^2/(2m_{i,\mathrm{eff}})$. However, at high effective carrier temperatures present shortly after photodoping, also the states far from the band minima are populated. To keep the total number of carriers in the simulation constant we numerically integrate the distribution function from Eq. (1) in momentum space and use the resulting carrier density $N_i(T_{\mathrm{eff}}) = \int_{-2\pi/a_0}^{2\pi/a_0} f(E_i(k), T_{\mathrm{eff}})dk$ to normalize the macroscopic intraband current of each band.

Data availability

All the data that support the plots and the other findings of this study are available from the corresponding author upon reasonable request.

Code availability

All the computational codes that were used to generate the data presented in this study are available from the corresponding author upon reasonable request.

Received: 14 February 2024; Accepted: 8 March 2024;
Published online: 21 March 2024

References

1. Brabec, T. & Krausz, F. Intense few-cycle laser fields: frontiers of nonlinear optics. *Rev. Modern Phys.* **72**, 545–591 (2000).
2. Corkum, P. B. & Krausz, F. Attosecond science. *Nat. Phys.* **3**, 381–387 (2007).
3. Hentschel, M. et al. Attosecond metrology. *Nature* **414**, 509–513 (2001).
4. Lewenstein, M., Balcou, P., Ivanov, M. Y., L'Huillier, A. & Corkum, P. B. Theory of high-harmonic generation by low-frequency laser fields. *Phys. Rev. A* **49**, 2117–2132 (1994).
5. Corkum, P. B. Plasma perspective on strong field multiphoton ionization. *Phys. Rev. Lett.* **71**, 1994–1997 (1993).
6. Ghimire, S. et al. Observation of high-order harmonic generation in a bulk crystal. *Nat. Phys.* **7**, 138–141 (2010).
7. Schubert, O. et al. Sub-cycle control of terahertz high-harmonic generation by dynamical Bloch oscillations. *Nat. Photon.* **8**, 119–123 (2014).
8. Luu, T. T. et al. Extreme ultraviolet high-harmonic spectroscopy of solids. *Nature* **521**, 498–502 (2015).
9. Vampa, G. et al. All-optical reconstruction of crystal band structure. *Phys. Rev. Lett.* **115**, 193603 (2015).
10. Vampa, G. et al. Linking high harmonics from gases and solids. *Nature* **522**, 462–464 (2015).
11. You, Y. S., Reis, D. A. & Ghimire, S. Anisotropic high-harmonic generation in bulk crystals. *Nat. Phys.* **13**, 345–349 (2016).
12. Liu, H. et al. High-harmonic generation from an atomically thin semiconductor. *Nat. Phys.* **13**, 262–265 (2016).
13. You, Y. S. et al. High-harmonic generation in amorphous solids. *Nat. Commun.* **8**, 724 (2017).
14. Yoshikawa, N., Tamaya, T. & Tanaka, K. High-harmonic generation in graphene enhanced by elliptically polarized light excitation. *Science* **356**, 736–738 (2017).
15. Wang, Z. et al. The roles of photo-carrier doping and driving wavelength in high harmonic generation from a semiconductor. *Nat. Commun.* **8**, 1686 (2017).
16. Hafez, H. A. et al. Extremely efficient terahertz high-harmonic generation in graphene by hot Dirac fermions. *Nature* **561**, 507–511 (2018).
17. Klemke, N. et al. Polarization-state-resolved high-harmonic spectroscopy of solids. *Nat. Commun.* **10**, 1319 (2019).
18. Ghimire, S. & Reis, D. A. High-harmonic generation from solids. *Nat. Phys.* **15**, 10–16 (2019).
19. Yang, Y. et al. High-harmonic generation from an epsilon-near-zero material. *Nat. Phys.* **15**, 1022–1026 (2019).
20. Jiang, S. et al. Crystal symmetry and polarization of high-order harmonics in ZnO. *J. Phys. B Atom. Mol. Opt. Phys.* **52**, 225601 (2019).
21. Yoshikawa, N. et al. Interband resonant high-harmonic generation by valley polarized electron–hole pairs. *Nat. Commun.* **10**, 3709 (2019).
22. Korobenko, A. et al. High-harmonic generation in metallic titanium nitride. *Nat. Commun.* **12**, 1–6 (2021).
23. Uzan, A. J. et al. Attosecond spectral singularities in solid-state high-harmonic generation. *Nat. Photon.* **14**, 183–187 (2020).
24. Lakhotia, H. et al. Laser picoscopy of valence electrons in solids. *Nature* **583**, 55–59 (2020).
25. Hollinger, R. et al. Carrier-envelope-phase measurement of few-cycle mid-infrared laser pulses using high harmonic generation in ZnO. *Opt. Express* **28**, 7314 (2020).
26. Heinrich, T. et al. Chiral high-harmonic generation and spectroscopy on solid surfaces using polarization-tailored strong fields. *Nat. Commun.* **12**, 3723 (2021).
27. Luu, T. T. & Wörner, H. J. Observing broken inversion symmetry in solids using two-color high-order harmonic spectroscopy. *Phys. Rev. A* **98**, 041802(R) (2018).
28. Lanin, A. A., Stepanov, E. A., Fedotov, A. B. & Zheltikov, A. M. Mapping the electron band structure by intraband high-harmonic generation in solids. *Optica* **4**, 516–519 (2017).
29. You, Y. S. et al. Laser waveform control of extreme ultraviolet high harmonics from solids. *Opt. Lett.* **42**, 1816 (2017).
30. Suthar, P., Trojánek, F., Malý, P., Derrien, T. J.-Y. & Kozák, M. Role of van Hove singularities and effective mass anisotropy in polarization-resolved high harmonic spectroscopy of silicon. *Commun. Phys.* **5**, 1–8 (2022).
31. Hohenleutner, M. et al. Real-time observation of interfering crystal electrons in high-harmonic generation. *Nature* **523**, 572–575 (2015).
32. Vampa, G. et al. Theoretical analysis of high-harmonic generation in solids. *Phys. Rev. Lett.* **113**, 073901 (2014).
33. Heide, C. et al. Probing electron-hole coherence in strongly driven 2D materials using high-harmonic generation. *Optica* **9**, 512–516 (2022).
34. Nagai, K. et al. Effect of incoherent electron-hole pairs on high harmonic generation in an atomically thin semiconductor. *Phys. Rev. Res.* **5**, 043130 (2023).
35. Bionta, M. R. et al. Tracking ultrafast solid-state dynamics using high harmonic spectroscopy. *Phys. Rev. Res.* **3**, 023250 (2021).
36. Peterka, P. et al. High harmonic generation in monolayer MoS_2 controlled by resonant and near-resonant pulses on ultrashort time scales. *APL Photon.* **8**, 086103 (2023).
37. Jeong, S., Zacharias, H. & Bokor, J. Ultrafast carrier dynamics on the Si(100)2 × 1 surface. *Phys. Rev. B* **54**, R17300–R17303 (1996).
38. Yoffa, E. J. Screening of hot-carrier relaxation in highly photoexcited semiconductors. *Phys. Rev. B* **23**, 1909–1919 (1981).
39. Goldman, J. R. & Prybyla, J. A. Ultrafast dynamics of laser-excited electron distributions in silicon. *Phys. Rev. Lett.* **72**, 1364–1367 (1994).
40. Sokolowski-Tinten, K. & von der Linde, D. Generation of dense electron-hole plasmas in silicon. *Phys. Rev. B* **61**, 2643–2650 (2000).
41. Aspnes, D. E. & Studna, A. A. Dielectric functions and optical parameters of Si, Ge, GaP, GaAs, GaSb, InP, InAs, and InSb from 1.5 to 6.0 ev. *Phys. Rev. B* **27**, 985–1009 (1983).
42. Sheik-Bahae, M., Said, A., Wei, T.-H., Hagan, D. & Van Stryland, E. Sensitive measurement of optical nonlinearities using a single beam. *IEEE J. Quant. Electron.* **26**, 760–769 (1990).

43. Kozák, M., Peterka, P., Dostál, J., Trojánek, F. & Malý, P. Generation of few-cycle laser pulses at 2 um with passively stabilized carrier-envelope phase characterized by f-3f interferometry. *Opt. Laser Technol.* **144**, 107394 (2021).
44. Kosik, E. M., Radunsky, A. S., Walmsley, I. A. & Dorrer, C. Interferometric technique for measuring broadband ultrashort pulses at the sampling limit. *Opt. Lett.* **30**, 326–328 (2005).

Acknowledgements

Czech Science Foundation (project GA23-06369S), Charles University (GAUK 349921, UNCE/SCI/010, SVV-2020-260590, PRIMUS/19/SCI/05). Funded by the European Union (ERC, eWaveShaper, 101039339). Views and opinions expressed are however those of the author(s) only and do not necessarily reflect those of the European Union or the European Research Council Executive Agency. Neither the European Union nor the granting authority can be held responsible for them. M.K. acknowledges the support of Czech Ministry of Education, Youth and Sports (project Terafit: CZ.02.01.01/00/22_008/0004594). T.J.-Y.D. acknowledges financial support from Czech Ministry of Education, Youth and Sports (project SenDiSo: CZ.02.01.01/00/22_008/0004596), and computational support from the e-INFRA CZ (ID:90254).

Author contributions

M.K. conceived and supervised the study. P.S. and M.K. performed the experiments and analyzed the experimental data. T.J.-Y.D. performed the band structure calculations. M.K. performed the numerical calculations. M.K. and P.S. wrote the manuscript with input from F.T., T.J.-Y.D., and P.M.

Competing interests

The authors declare no competing interests.

Additional information

Supplementary information The online version contains supplementary material available at https://doi.org/10.1038/s42005-024-01593-x.

Correspondence and requests for materials should be addressed to Martin Kozák.

Peer review information *Communications Physics* thanks the anonymous reviewers for their contribution to the peer review of this work.